



Hierarchical zero- and one-dimensional topological states in symmetry-controllable grain boundary

Received: 26 December 2023

Accepted: 7 October 2024

Published online: 29 October 2024

Won-Jun Jang ^{1,7}, Heeyoon Noh ^{2,7}, Seoung-Hun Kang ³, Wonhee Ko ⁴, JiYeon Ku¹, Moon Jip Park ^{5,6}  & Hyo Won Kim ¹ 

Structural imperfections can be a promising testbed to engineer the symmetries and topological states of solid-state platforms. Here, we present direct evidence of hierarchical transitions of zero- (0D) and one-dimensional (1D) topological states in symmetry-enforced grain boundaries (GB) in 1T'-MoTe₂. Using a scanning tunneling microscope tip press-and-pulse procedure, we construct two distinct types of GBs, which are differentiated by the underlying symmorphic and nonsymmorphic symmetries. The GBs with the non-symmorphic rotation symmetry harbor first-order topological edge states protected by a nonsymmorphic band degeneracy. On the other hand, the edge state of the symmorphic GBs attains a band gap. More interestingly, the gapped edge state realizes a hierarchical topological phase, evidenced by the additional 0D boundary states at the GB ends. We anticipate our experiments will pioneer the material platform for the hierarchical realization of first-order and higher-order topology.

The topology of the electronic band is an essential factor in understanding the materials' electrical and quantum properties. Bulk-boundary correspondence, as a guiding principle of the topological phase, dictates the intimate relationship between the topological invariant of bulk and the metallic excitations at the boundary^{1–3}. A prototypical example of materials with non-trivial topology is found in topological insulators (TIs), which have inverted band gaps by large spin-orbit coupling and topological character protected by time-reversal symmetry^{4–7}. Moreover, a larger class of topological materials is available when we add crystalline symmetries, exemplified by topological crystalline insulators (TCIs)^{8,9} and higher-order topological insulators (HOTIs)^{10–13}. HOTIs are especially interesting because they broaden the concept of bulk-boundary correspondence not to be limited between N -dimensional bulk and $(N-1)$ -dimensional boundary, but to be applicable between N -dimensional bulk and $(N-n)$ -dimensional boundaries with $n > 1$. For example, second-order HOTI with 3D

(2D) bulk should have topologically protected 1D hinge (0D boundary) states.

Observing topological boundary states is a key to identifying the non-trivial bulk topology. Crystallographic defects such as lattice dislocations and grain boundaries (GBs) are of particular interest since they can trap the localized boundary states. The topological protection of the boundary state depends on the crystal symmetry and the dimensionality of both the parent topological state and the defect^{14–20}. In the case of 2D and 3D HOTI, realizing variant crystallographic defects provides a promising route to engineer topological boundary states by creating different types of defects that either preserve or break the underlying crystalline symmetries²¹. With a local probe that can characterize and manipulate these crystallographic defects, we can identify the non-trivial topology of the bulk as well as control the topological states by the symmetry of defects^{22–24}.

¹Samsung Advanced Institute of Technology, Suwon 16678, Korea. ²Department of Physics, Yonsei University, Seoul 03722, Korea. ³Materials Science and Technology Division, Oak Ridge National Laboratory, Oak Ridge, TN 37831, USA. ⁴The Department of Physics and Astronomy, University of Tennessee at Knoxville, Knoxville, TN 37996, USA. ⁵Center for Theoretical Physics of Complex Systems, Institute for Basic Science (IBS), Daejeon 34126, Republic of Korea. ⁶Department of Physics, Hanyang University, Seoul 04763, Korea. ⁷These authors contributed equally: Won-Jun Jang, Heeyoon Noh.

 e-mail: moonjippark@hanyang.ac.kr; hyowon98.kim@samsung.com

A scanning tunneling microscope (STM) is a unique atomic-scale microscopy tool that has been extensively used for observing topological states^{1,2} as well as manipulating them with atom manipulation techniques²⁵. The precise control of the bias pulse and the sample-tip distance allows STM to manipulate individual atoms and defects with atomic precision. However, the application of such nanoscale manipulation to HOTI and demonstration of hierarchical topological states with respect to the symmetries are challenging, because it requires finding the right bulk materials with non-trivial topology that at the same time can be manipulated by STM to create atomic defects with suitable crystalline symmetries.

In this work, we apply the tensile strain on 1T'-MoTe₂ by poking the surface with an STM tip in a controlled fashion to create and stabilize symmetry differentiable GBs. The boundary matching of the atomic structure admits the two possible types of GBs, each of which is characterized by the distinct crystalline symmetries along the GBs: symmorphic C₂- (SymC2) and non-symmorphic C₂- (NonSymC2) rotational symmetries. The strain induces domain switching between three orientation variants of the 1T' phase and creates symmetry-dictated GBs^{1,26}. To create GBs, we design a new STM manipulation method that induces ferroelastic switching between three orientational variants of the 1T' phase of MoTe₂ in a controlled and

reproducible way. The GBs created by STM manipulation exhibit different topological states depending on a type of crystalline symmetry, i.e. the 1D topological edge states and the 0D topological boundary states for non-NonSymC2 and SymC2 rotational symmetries, respectively. Our results demonstrate that STM manipulation is a promising route to achieve the controllable manipulation of the HOTI states by ferroelastic switching.

Results

Creation of symmetry-enforced grain boundaries

Due to the quantum spin Hall phase of 1T'-MoTe₂, the GBs of 1T'-MoTe₂ harbor the pair of helical edge states originating from each side of the quantum spin Hall insulating bulk. In general, these pairs can be gapped out, but NonSymC2 GBs stabilize the double helical edge mode, whose band degeneracy is protected by the non-symmorphic symmetry (Fig. 1a top)¹⁶. On the other hand, the SymC2 GBs lose their topological protection and acquire a finite band gap. Nevertheless, SymC2 symmetry gives rise to the higher-order topological classifications of the gapped edge. The resulting electronic states of the SymC2 GB are analogous to the well-known Su-Schrieffer-Heeger chain²⁷, which manifests as the 0D boundary states (Fig. 1a bottom)²⁸.

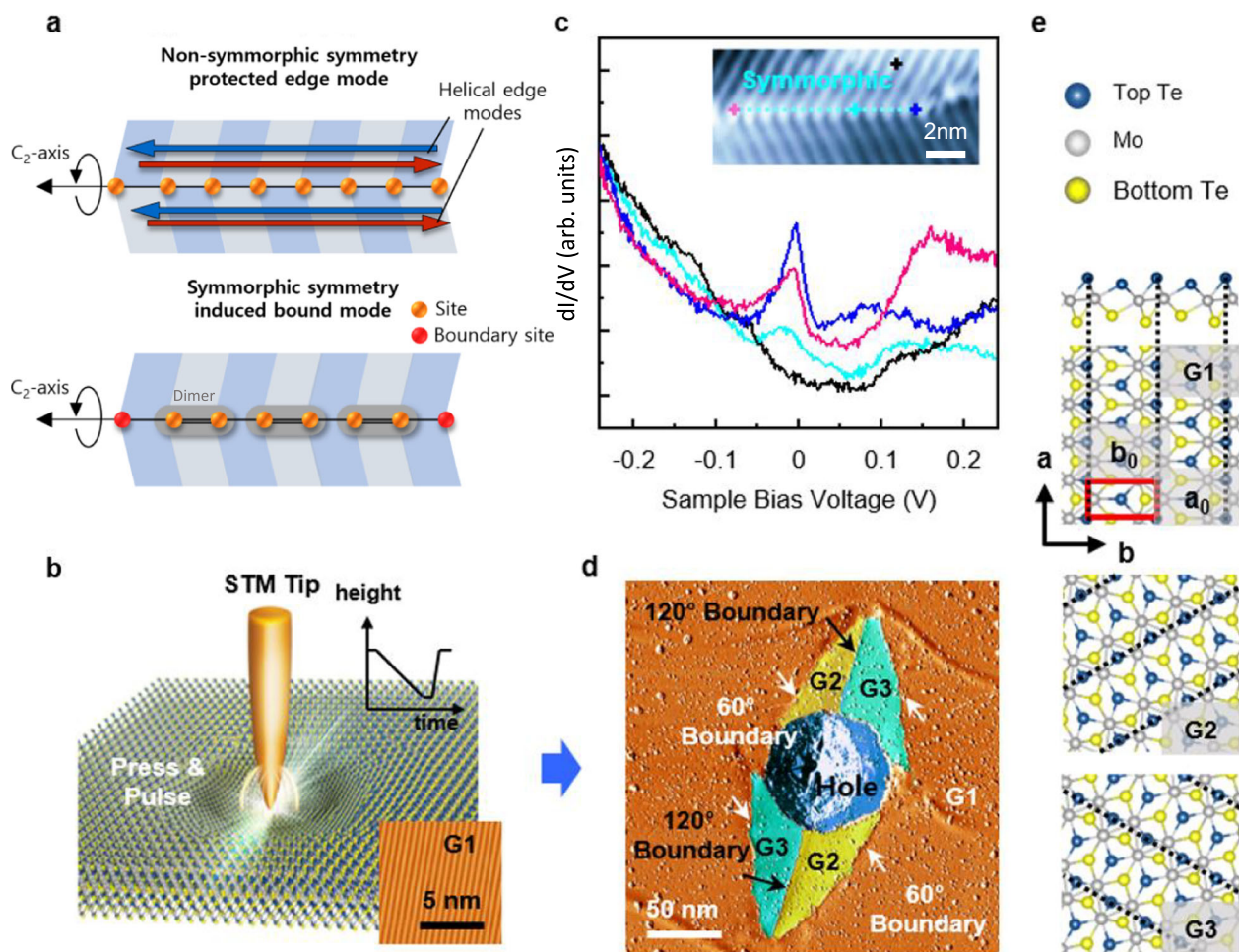


Fig. 1 | Hierarchical zero- and one-dimensional topological states in symmetry-enforced grain boundaries (GB) of 1T'-MoTe₂. **a** Illustration of topological states in non-symmorphic and symmorphic GBs. While the non-symmorphic GBs have protected edge modes, the symmorphic GBs allow atomic dimerizations, which give rise to the zero-dimensional higher-order topological states. **b** Schematic illustration for the GB formation process of GBs using an Scanning Tunneling Microscopy (STM) tip. Inset: Derivative STM image of pristine

1T'-MoTe₂ surface showing quasi-one-dimensional chains formed by the Te atoms and denoted the region of this original chain direction as G1. **c** dI/dV spectra taken at the positions indicated by the black, cyan, magenta, and blue dots in the inset. Inset: STM image showing a 120° SymC2 GB created in 1T'-MoTe₂. **d** Derivative STM image of 1T'-MoTe₂ obtained after GBs formation process. **e** Structural models of the 1T'-MoTe₂, denoted as G1, G2 and G3. The Te chain directions are marked by the dotted lines to help guide the eyes.

To create such GBs and to characterize their atomic and electronic structures, we employ STM and scanning tunneling spectroscopy (STS). A tensile strain can be applied by pressing the STM tip to the surface, and furthermore, electrical and/or thermal energy can be transmitted by applying a tip voltage pulse at a desired position (Fig. 1b). Inset of Fig. 1c shows a representative topographic image of the SymC2 GB between NonSymC2 GBs created by such STM manipulation. The differential conductance (dI/dV) spectra in Fig. 1c show a strong contrast between the ones taken at the center of GB (cyan), ends of GB (magenta and blue), and bulk (black), which we will later show to originate from the topological boundary states of SymC2 GB. Figure 1d shows a representative large-scale derivative STM image of the strain-engineered GBs in $1T'$ - MoTe_2 . In the pristine surface of $1T'$ - MoTe_2 , the Te atoms form quasi-one-dimensional chains with a preferred direction due to the dimerization of Mo atoms from the high symmetry phase (1T) (denoted by region G1 in Fig. 1b). By pressing the STM tip to the surface with applying a voltage pulse of -2.5 V, the pressed G1 region transforms to the diamond shape of different types of grains (G2 and G3) (Fig. 1d), corresponding to the two of the other six-fold rotation variants of the $1T'$ phase with different Te-chain direction (Fig. 1e).

To characterize the optimal condition for obtaining the grain-switched diamond-shaped structure shown in Fig. 1d, we investigated several experimental parameters: (1) applied voltage pulse (V_p); (2) depth of surface indentation (D , which is defined as the distance after the tunneling current reaches 100 nA. For delicate control of D , we used z-spectroscopy before every switching process, and D was varied from a few angstroms to 30 nm); (3) time to lower the tip to the surface (T_1 , varied from 0.5 s to 10 s); (4) duration at the lowest position for tip pulse (T_2 , varied from 0.2 to 0.5 s); and (5) time to lift the tip (T_3 , varied from 0.02 s to 10 s.). The various results from changing the parameters are presented in the Supplementary Information. Subsequently, we determined the following optimal condition: $V_p = -2.5 \sim -3$ V, $D = -0.1 \sim -0.2$ nm, $T_1 = 0.5 \sim 3$ s, $T_2 = 200$ ms and $T_3 = 20$ ms (Supplementary Fig. S2). We note that applying only voltage pulse V_p did not generate new grains, and applying tensile strain by pressing down the surface with certain D and T_1 is essential to form the diamond-shaped structure. Further details of their dependence are presented in Supplementary Note 2 and Figs. S2–S6. Many additional examples of the control of GBs are provided in the Supplementary Information.

Hierarchical 0D and 1D topological states

The relative angles of Te-chain directions characterize the GBs between each region. Adjacent G2 and G3 grains bear a GB with the angle of 120° (G2–G3), and G2 and G3 regions form mostly GB with the angles of 60° with respect to the original G1 phase (G1–G2 and G1–G3) (See supplementary Fig. S7 for full geometric characterizations of the GBs and Supplementary Figs. S12–15 for geometric and electronic properties of 60° GBs). Further inspection of the STM image on the 120° boundary reveals the coexistence of both the NonSymC2 and SymC2 GBs (Fig. 2a). Furthermore, the distinctive behaviors in the dI/dV spectra are identified for different GBs. The dI/dV spectrum at the NonSymC2 GB, marked by the dotted orange line in Fig. 2a (also shown as the orange line in Fig. 2b), reveals a differential conductance peak near $+28$ mV, whereas no such features are shown inside the grain far away from GBs (black line in Fig. 2b) as well as the SymC2 GB (cyan line in Fig. 2b).

The atomic configurations of both types of 120° GBs are characterized by a C2 rotation along the y-axis, offering greater energetic stability compared to the y-axis mirror reflection in 120° GBs¹⁸. These configurations can be further categorized into NonSymC2 and SymC2 based on the presence or lack of half translation, illustrated in Supplementary Fig. S8a, c. Their electronic properties are depicted in Supplementary Fig. S8b, d. The gapless metallic states originate from

the non-trivial Z_2 index of the quantum spin Hall insulator phase of MoTe_2 . In general, the double helical edge mode originating from the left, and the right side of the domain can be trivially gapped out. Nonsymmorphic symmetry further protects the gapless crossings characterized by the bow-tie types band structure. Unlike the non-symmorphic GB, the topological protection of the gapless state is removed at the symmorphic GB.

The spatial dI/dV maps of the 120° GB clearly show the 1D boundary state at the NonSymC2 GBs (Fig. 3c). The boundary mode is well-localized at the NonSymC2 GB as seen in the dI/dV map acquired at 34 mV in the upper right panel in Fig. 3c (further dI/dV maps are presented in Supplementary Fig. S9). The observed boundary mode in the NonSymC2 GB agrees with the theoretically predicted bowtie shape in-gap metallic states (Fig. 2e). The boundary states originated from the pair of the helical edge states of each quantum spin Hall grain. In general, these boundary states are allowed to be gapped out by the interactions between the helical edges, since each side of the GB has the same Z_2 index. However, the additional NonSymC2 symmetry gives rise to the Young–Kane type non-symmorphic band degeneracy²⁹, which protects the band crossings of the double-helical edge states.

In contrast, the SymC2 GB shows no sign of the in-gap edge states, and it suggests the avoided level crossings between edge modes in the absence of symmetry protection. However, interestingly, the measured dI/dV spectrum at the end of SymC2 GB (violet line in Fig. 3b) reveals the additional peak near -4 mV (further clearly shown in the dI/dV spectra in Fig. 1c). The peaks are spatially localized at both ends of the GBs, as shown in the spatial dI/dV map in the left panel in Fig. 3c, and it signifies the presence of the 1D boundary states. The peaks are slightly broadened due to the finite size effect. A sharper peak is shown in the Fig. 3g, measured in longer GB in Fig. 3e. The corresponding dI/dV maps obtained at -4 and 34 mV are presented in Fig. 3f.

Our theoretical calculation also verifies the gapped spectra of the edge mode (Fig. 2g). Further symmetry analysis reveals the higher-order topological classifications of the edge mode. The approximate inversion symmetry along the grain boundary and chiral symmetry gives Z_2 classification of the gapped 1D edge (AIII class). (See supplementary Information for other AI topological classification). The corresponding symmetry classification is formally equivalent to that of the SSH model, where the dimerizations of the hoppings give rise to the unpaired boundary states at each end³⁰. In SymC2 GB, the dimerization of the Mo atoms (shown by the green stripes in Supplementary Fig. S17) gives rise to the effective dimerization of the hoppings. Using the effective model, we also calculated local density of states (LDOS) near both SymC2 and NonSymC2 GBs (Supplementary Figs. S20, S21).

To confirm that the 0D states are not artifacts of the states in the adjacent NonSymC2 GBs, we examined the possible hybridization between the 1D topological boundary states in NonSymC2 GBs and the 0D boundary states in SymC2 GBs. Despite their positional proximity, the dI/dV map on the side of the NonSymC2 GBs shows a diminishing amplitude as it approaches the end of the chain. This behavior resembles a typical quantum confinement phenomenon^{31–33}, with negligible hybridization with the 0D states. Consequently, we conclude that there is vanishing tunneling of the 0D boundary state to the NonSymC2 GBs, confirming that the 0D boundary states are intrinsic to the SymC2 GBs and are not influenced by the adjacent NonSymC2 GBs. We can read out information about the hybridization by analyzing the confined state by analyzing NonSymC2 GBs with a finite length (Fig. 4a). The dI/dV maps reveal the quantum well-like resonant bound states with the first ($n=1$) and the second harmonics ($n=2$) for the corresponding applied bias voltages 20 mV and 58 mV, respectively (Fig. 4b). The change of the LDOS maxima depending on the measured position within the NonSymC2 GB shown in a series of dI/dV spectra in Fig. 4c exhibits a typical quantum confinement phenomenon^{3–5}. These

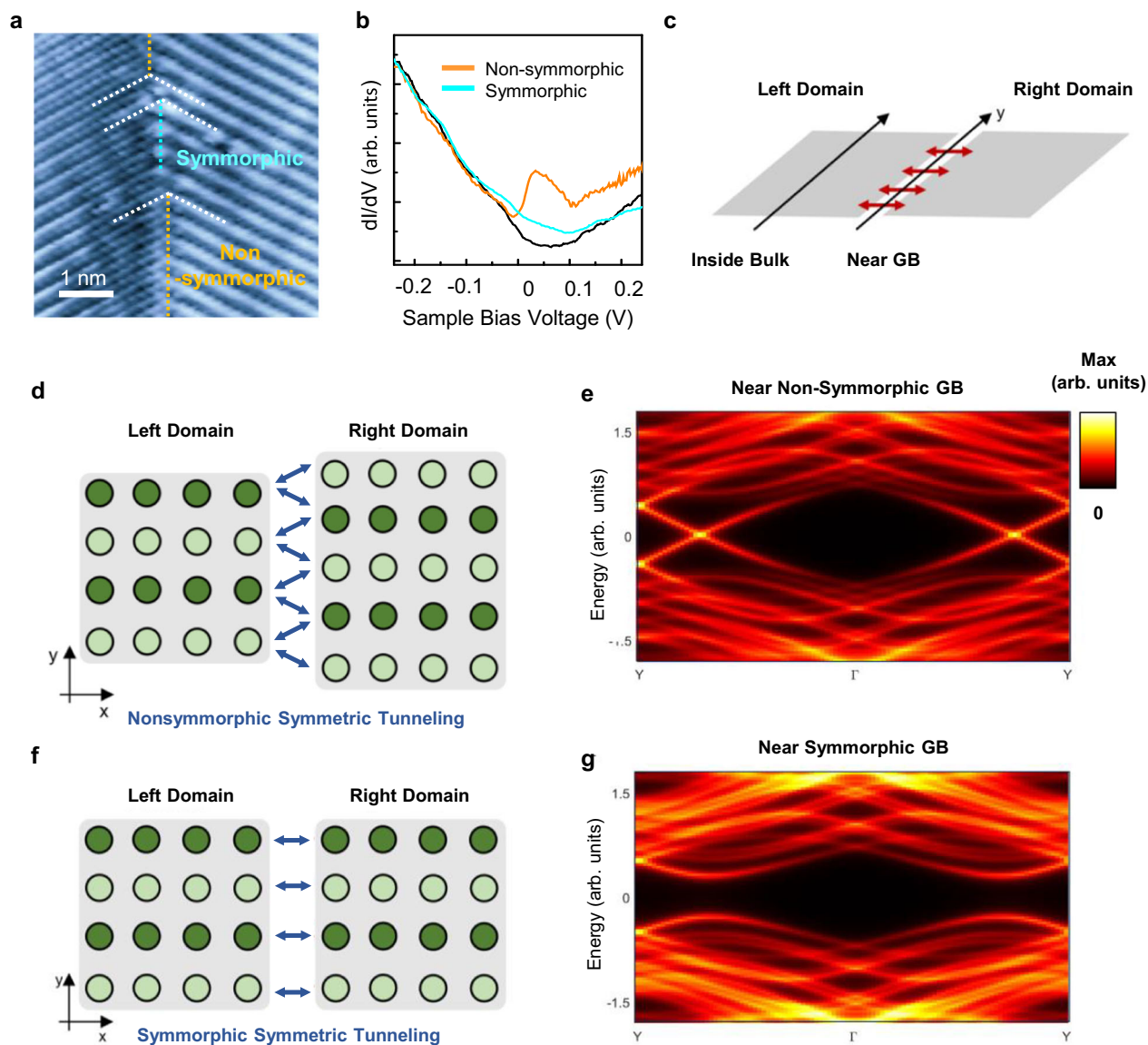


Fig. 2 | Morphology and electronic structure of 120° GBs created in 1T'-MoTe₂. **a** STM image of the 120° GBs ($V_s = -20$ mV, $I = 0.7$ nA). **b** dI/dV spectra obtained at the non-symmorphic C2- (NonSymC2) GB (orange), symmorphic C2-(SymC2) GB (cyan), and right area (black). **c** Schematic illustration of the GB geometry

used in the numerical calculation. **d, f** Schematic illustration of the GB and non-symmorphic and symmorphic symmetric tunneling, respectively. **e, g** LDOS calculated near the non-symmorphic GB and near the symmorphic GB, respectively.

confinements are clearly observed in the dI/dV line profiles in Fig. 4d. The wave function of the confined state with $n = 1$ vanishes strongly at both ends of the NonSymC2 GB, which indicates the physical separation from that of the SymC2.

Discussion

Controllability of GB creation and the underlying mechanisms

Wenbin Li and Ju Li theoretically predicted that only mechanical strain can derive the 1T'-to-1T' phase transition²⁶. In particular, they demonstrated that a few percent of biaxial supercell strain induce variant switching from G1 to G2/G3. As we mention above, we also attempted to apply tensile strain without a voltage pulse. However, the surface of MoTe₂ did not show grain switching. We hypothesized that although grain switching occurred when pressing the surface, the switched grains, G2 and G3, reverted to G1, after the tip detached from the surface. Therefore, we surmised that applying a bias voltage and resultant a hole play a key role to preventing the switched grains from

reverting. The voltage pulse transmitted from the tip to the surface created an electric field, which initially facilitated hole formation and then assisted in switching the grains.

Our several experimental results support this scenario in several ways. First, the grain-switched diamond-shaped structures are created with only at certain bias voltages, specifically $V_p = -2.5$ to -3 V, which are appropriate for creating a hole and switching the grains. If the bias of voltage is not sufficient to facilitate to switching the grain, the switching does not occur. Thus, with -2.0 V $< V_p < 0$ V, only holes are created without any grain formation, as we noted in previous Supplementary Note 1. Similarly, with $-2.0 < V_p < -2.5$ V, G2 and/or G3 are occasionally formed, but not the diamond shape as shown in Fig. 1d.

Second, the scenario is further supported by the GB formation mechanism due to the in-plane electric field in Fig. 5. In this method, we first created a hole by pressing and applying a voltage pulse with an STM tip, and then positioned the tip at the center of the hole to touch

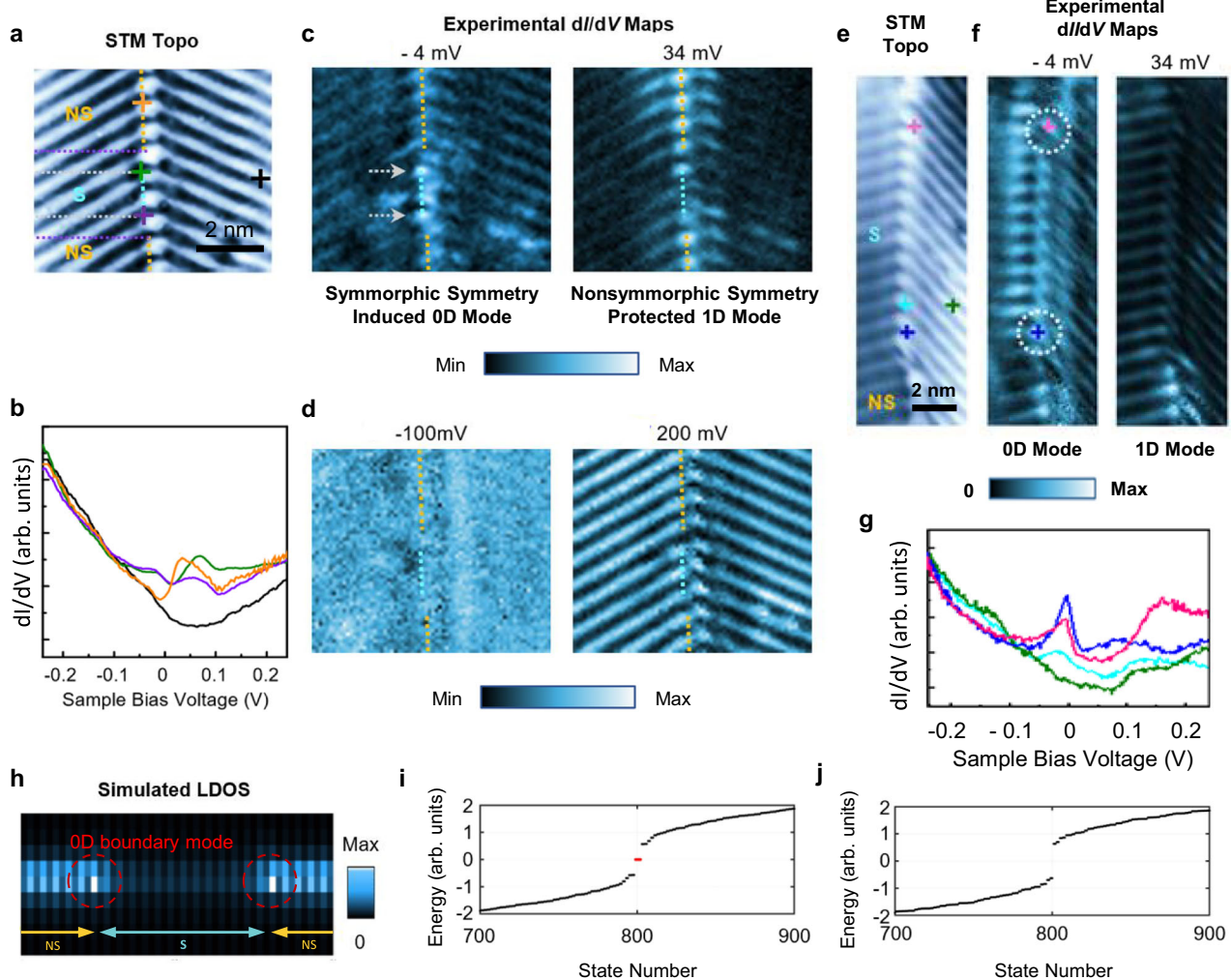


Fig. 3 | LDOS maps of SymC2 symmetry-induced 0D modes and their finite length effects, and NonSymC2 symmetry-protected 1D modes. **a** STM image of $1T'$ - MoTe_2 with a SymC2 GB surrounded by two NonSymC2 GBs ($V_s = -240$ mV, $I = 0.1$ nA). **b** dI/dV spectra taken at the position indicated by the colored crosses in **(a)**. **c, d** dI/dV maps obtained over the area shown in **(a)** for bias voltages $V_s = -100, -4, 34$ and 200 mV. The dotted white arrows in the upper left indicate S symmetry-induced boundary modes. **e** STM image of $1T'$ - MoTe_2 with a longer SymC2 GB near NonSymC2 GBs ($V_s = -240$ mV, $I = 0.1$ nA). **f** dI/dV maps obtained over the area shown in **(e)** for bias voltages $V_s = -4$ and 34 mV.

g dI/dV spectra taken at the positions indicated by the black, cyan, magenta, and blue dots. **h** Numerically calculated NonSymC2-SymC2-NonSymC2 junction of the GBs. Due to the non-trivial band gap of the SymC2 boundary, we find the emergence of the higher-order topological boundary states at the end of the SymC2 GBs. **i–j** Energy spectra of the SymC2 GB in the open and periodic boundary conditions respectively. In the open boundary condition, the one-dimensional boundary harbors the additional zero-dimensional higher-order topological states (red dots). A total of four states appears, and two of them are localized at each end of the chain.

the edges of holes, as shown in Fig. 5a³⁴. Lowering the tip slightly allowed full contact between the circumference of the tip and the edge of the previously created hole. Note that this depth is defined from the distance between 1 and 2 in Fig. 5c. When a voltage pulse is applied, the electric field is applied along the in-plane direction and inducing electrically strain-driven phase switching. As a result, the characteristic diamond structure is formed without any mechanical stress. A more delicately controlled GB formation method shown in Fig. 5b further enabled probing the effect of in-plane electric field on the GB switching. We placed the tip very close to the upper side of the edge, as indicated by the red cross in Fig. 5d. Then, we applied a voltage pulse to create GBs. As a result, we obtained only the upper half of the previously observed diamond structure, because grain switching occurred only in the region next to the contact between the tip and the hole edge (Fig. 5e). The result substantiates that electric field-induced phase switching requires a pre-existing hole structure with exposed step edges, which allows the pulse from the tip to transmit the strain in the in-plane direction.

Third, the diamond-shaped structure indicates that grain switching depends significantly on the in-plane structural anisotropy of $1T'$ - MoTe_2 . All grain switching preferably occurs along the Te rows (a direction) and, consequently, produces the diamond-shaped structure. This suggests that the structural anisotropy of $1T'$ - MoTe_2 on the surface affects electrical conductivity and elastic properties on the surface. In the previous reports, the electric conductivity of $1T'$ - MoTe_2 exhibits anisotropic behavior, with conductivity along the a direction being approximately twice as high as in the b direction at 10 K³⁵. Consequently, transmitted bias voltage more quickly propagates along the a direction than the b direction. Density functional theory (DFT) calculations were conducted to investigate the response of the lattice structure to an external electric field. Starting from the fully optimized MoTe_2 structure, the lattice constant in one direction was held fixed while the other was allowed to relax under an external field applied along the Te row (a direction). The percent differences in the relaxed lattice constants, relative to the optimized structure in the absence of the field, were calculated (Fig. 5i). The

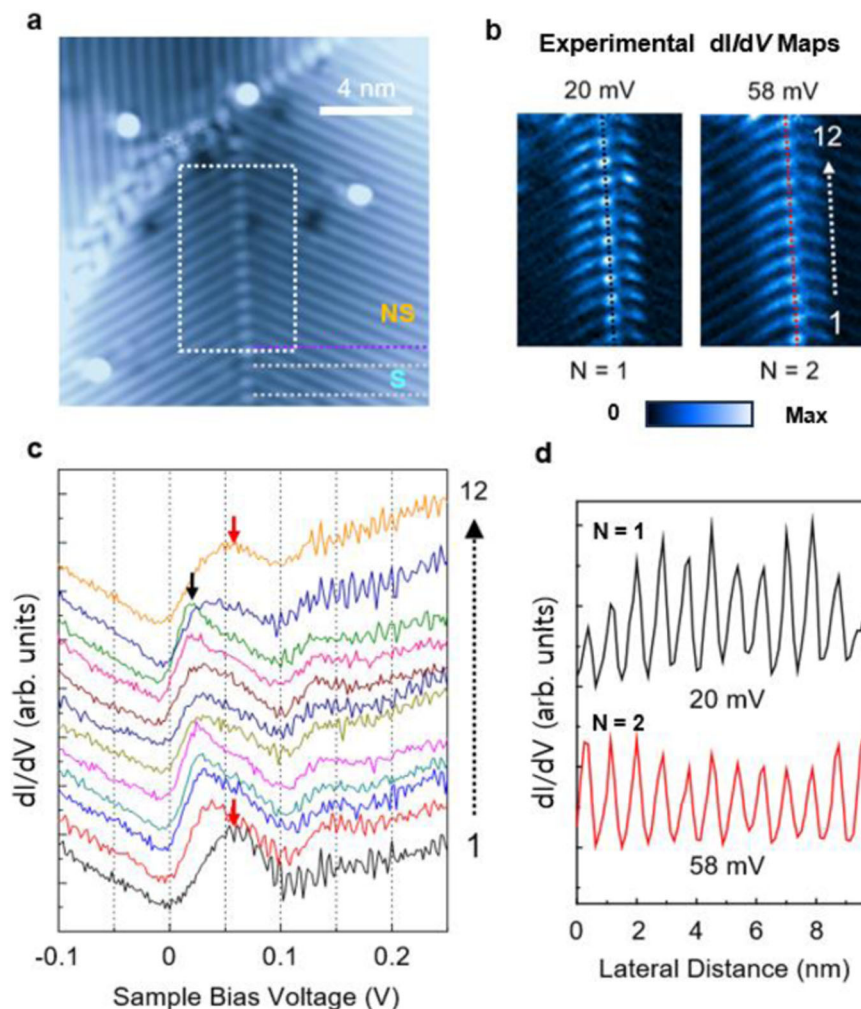


Fig. 4 | Quantum confinement effects in the NonSymC2 GB with finite length adjacent SymC2 GB. **a** STM image of 1T'-MoTe₂ with NonSymC2 and SymC2 GB ($V_s = -240$ mV, $I = 0.1$ nA). **b** dI/dV maps obtained in the NonSymC2 GB for bias

voltages $V_s = 20$ mV and 58 mV. **c** dI/dV Spectra acquired along the NonSymC2 GB from 1 to 12 marked in the right in (**b**). **d** LDOS line profiles of the NonSymC2 GB at the energies of $N=1$ and $N=2$, acquired along the dotted black and red lines in (**b**).

results reveal that the lattice constant in the a direction increased, indicating a stretching effect, while the b direction contracted, demonstrating that the external electric field induces anisotropic deformation in the lattice.

This spatially anisotropic grain formation is further confirmed by additional experiments. We placed the STM tip for voltage pulsing at the edge of the existing hole as indicated by the red cross in Fig. 5g. In this case, the tangent to the circular hole at the tip position lies parallel to the Te rows, and the electrically applied stress across the Te chains does not induce strain or grain switching. Instead, it causes structural damage by removing atomic layers and creating an additional hole (Fig. 5h).

The anisotropy of the elasticity in a and b directions of MoTe₂ also affects on the determination of the shape of grain switching³⁶. We calculated the ratio of the extensions in the a and b directions when the surface is pressed along the c direction³⁶. Upon applying a uniaxial strain ϵ_z in the c direction, the ratio of the extensions in the b and a direction is $\frac{\epsilon_a}{\epsilon_b} \approx 1.316$ (Details see Supplementary Note 3). This result indicates that the a direction is further extend although we pressed the surface z direction. These anisotropic properties are intrinsically governed by the inherent characteristics of the material.

To the control the transition between SymC2 and NonSymC2, we performed additional experiments. After obtaining GBs through

the same formation process, we pressed on the indicated position in Fig. 6a with an STM tip, without applying a pulse. We discovered that the upper part of the GB moved as shown in Fig. 6b, and the dI/dV spectra revealed that the NonSymC2 GB changed to the SymC2 GB (Fig. 6c, d). These results indicate that, although our GB formation process cannot initially selectively create SymC2 and NonSymC2 GBs, the transition between the two can be controlled through tensile strain, as predicted by the theoretical results of Wenbin Li and Ju Li²⁶. In addition, we note that the newly created SymC2 in Fig. 6b is very short. As a results, the dI/dV spectrum (cyan line) measured in the center of the GB shows the broadening effect of the OD modes at its ends.

In conclusion, we demonstrate hierarchical 0D and 1D topological states created in the NonSymC2 and SymC2 GBs created in a 1T'-MoTe₂ by mechanically and electrically induced tensile strain using the STM tip. While the 1D topological edge mode appears on the NonSymC2 GB, the SymC2 GB attains the topological band gap and realizes the higher-order topological states at the GB ends. HOTIs have been theoretically well studied, however, their experimental observations have been rarely reported^{37,38}. Thus, our experimental demonstration not only provides direct evidence for the physical realization of higher-order topological states but also a new method for creating and controlling symmetry-dictated GBs.

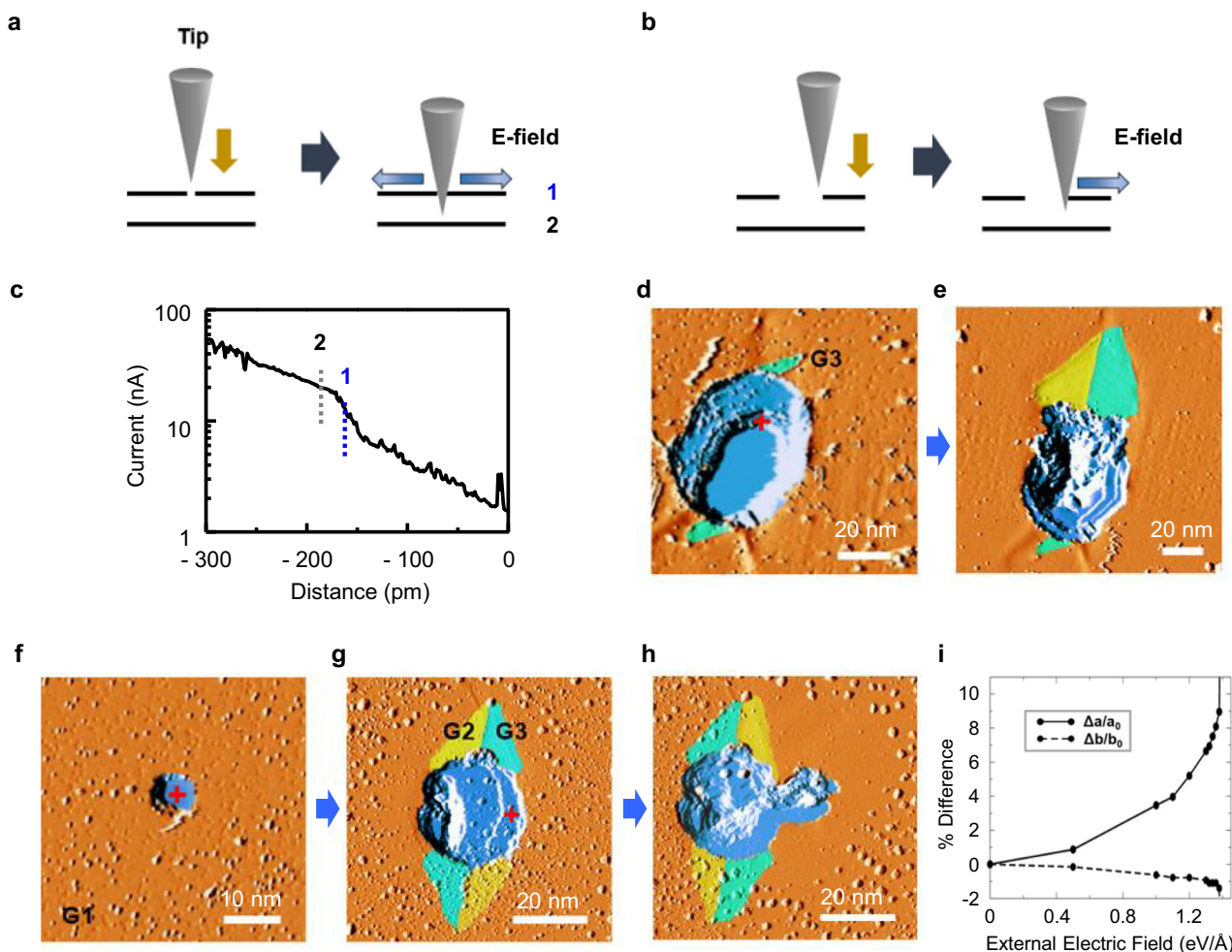


Fig. 5 | Electric-field induced GB formation of 1T'-MoTe₂. **a, b** Side view of schematic illustrations of the GB formation processes by creating a hole on the surface, contacting the hole edge with an STM tip, and applying a voltage pulse. **c** Current trace as a function of tip-approaching distance. **d, f** Derivative STM images obtained after a hole creation. **e, g** Derivative STM images taken after the GB formation process performed at the position marked with the red cross in (d), and

(f) via the method illustrated in (a) and (b), respectively. **h** Derivative STM images taken after the grain-switching process performed at the position marked with the red cross in (g). **i** DFT-calculated changes in the cell parameters vs. external electric field along the *a* and *b* axes, where *a*₀ and *b*₀ are the optimized lattice constants calculated without any constraints.

Methods

Scanning tunneling microscopy/spectroscopy measurement

We performed the experiments in two commercial low-temperature STM instruments (RHK and Unisoku operated at 4.2 K and 2.8 K, respectively.) in an ultrahigh vacuum (pressure < 1.0 × 10⁻¹⁰ Torr). 1T'-MoTe₂ single crystal samples were purchased from HQ Graphene. The sample was cleaved in an ultrahigh vacuum chamber (~10⁻¹⁰ Torr) at room temperature and then transferred to the low-temperature STM sample stage, where the temperature was kept at 4.2 K or 2.8 K.

Tight-binding model of 1T'-MoTe₂

To study the electronic structure of the topological edge state, we construct the Slater-Koster type tight-binding model from the DFT based band structure. We have derived the tight-binding band structure of 1T'-MoTe₂ based on the DFT model with three p-orbitals for Te-atoms and five d-orbitals for Mo-atoms. The tight-binding model in real space is generally written as,

$$H = \sum_{i,j} \sum_{\alpha, \alpha', \sigma, \sigma'} t_{ij}^{\alpha, \alpha'} c_{i\alpha\sigma}^\dagger c_{j\alpha'\sigma'} + H_{SOC}.$$

Here, *i, j* represent the site index for each atom. *α, α'* represent the orbital degree of the freedom. For instance, in the case of Mo atoms, *α, α'* = *d_{xy}, d_{yz}, d_{zx}, d_{x²-y²}, d_{3z²-r²}*. In the case of Te atoms *α, α'* = *p_x, p_y, p_z*. *t_{ij}^{α, α'}* is the transfer matrix, which is calculated from the Slater-Koster formula. *H_{SOC}* is the onsite spin-orbit coupling term.

Band structure and Z₂ topological invariant

Z₂ topological invariant, *ν*, can be calculated by the Fu-Kane formula as,

$$(-1)^\nu = \prod_i \delta_i, \quad \delta_i = \prod_m \xi_{2m}(\Gamma_i)$$

where *ξ_{2m}(Γ_i)* is the inversion eigenvalue of 2*m*-th occupied bands at the time-reversal invariant momenta Γ_i. Due to the time-reversal and inversion symmetry, the band structure has the Kramers degeneracy at the momenta. The number of inversion-odd occupied band is summarized in Table 1, which results in the non-trivial Z₂ invariant. The non-trivial Z₂ invariant is the robust quantity even in the presence of the inversion symmetry breaking perturbation as long as the perturbation does not induce the additional band gap closing.

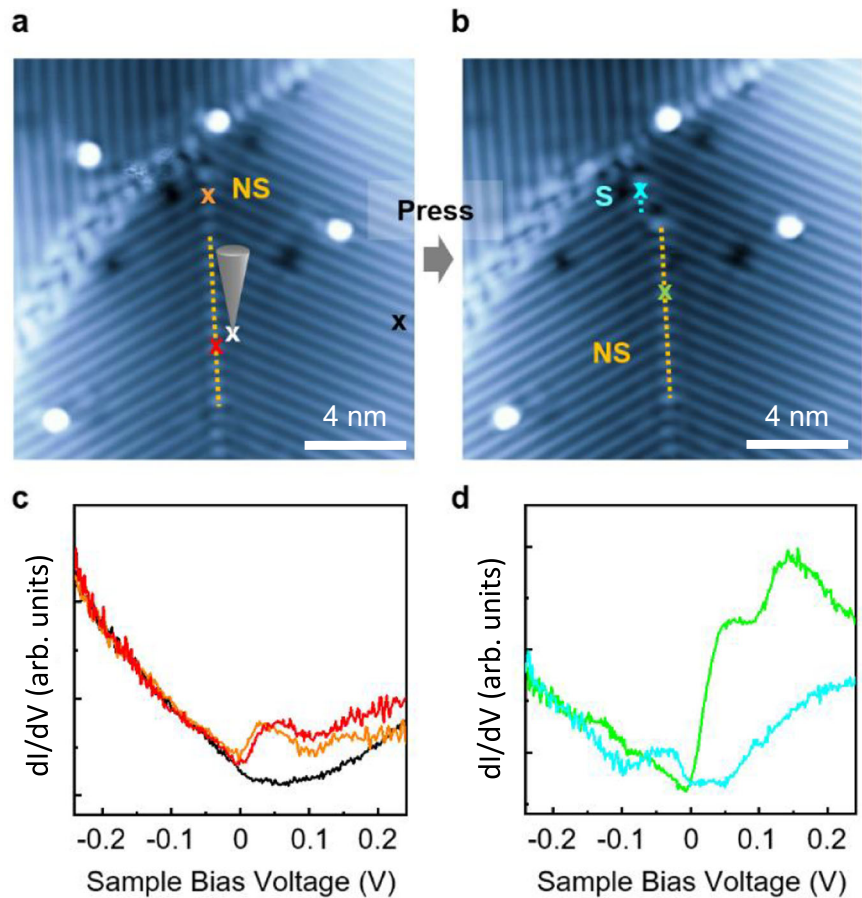


Fig. 6 | Manipulation from the NonSymC2 to the SymC2 GBs. **a** STM image showing a NonSymC2 GB created in 1T'-MoTe₂. **b** STM image obtained after pressing the marked with an X in **(a)** by a STM tip. **c** dI/dV spectra obtained at the NonSymC2 (orange and red) GB. **d** dI/dV spectra at the NonSymC2 (green) and SymC2 (cyan) GBs.

Table 1 | Calculated inversion eigenvalues of the occupied bands

Momenta	(0, 0)	(π , 0)	(0, π)	(π , π)
Number of occupied bands	12	14	14	14

The non-trivial topological invariant can be further examined by showing the edge states with the open boundary condition. Supplementary Fig. 1 compares the energy spectra in the closed and open boundary conditions respectively. The emergence of the edge spectra confirms the non-trivial topological invariant.

Density functional theory calculations

DFT calculations were carried out using the Vienna ab initio simulation package (VASP) employing the generalized gradient approximation (GGA) with Perdew-Burke-Ernzerhof (PBE) exchange-correlation functional form and the projector-augmented wave methods^{39–43}. For all calculations, wave functions were expanded in plane waves with the cutoff energy of 350 eV, and the atomic positions were relaxed until the residual forces were less than 0.02 eV/Å or until the change of the total energy was less than 1.0×10^{-6} eV. All calculations were performed using a 1T'-MoTe₂ monolayer, and a vacuum of at least 20 Å was applied to the cell to prevent interaction between the slabs.

Data availability

The data that support the findings of this study are available from the corresponding author upon request.

References

- Hasan, M. Z. & Kane, C. L. Colloquium: Topological insulators. *Rev. Mod. Phys.* **82**, 3045 (2010).
- Qi, X.-L. & Zhang, S.-C. Topological insulators and superconductors. *Rev. Mod. Phys.* **83**, 1057 (2011).
- Isaev, L., Moon, Y. H. & Ortiz, G. Bulk-boundary correspondence in three-dimensional topological insulators. *Phys. Rev. B* **84**, 075444 (2011).
- Kane, C. L. & Mele, E. J. Quantum spin hall effect in graphene. *Phys. Rev. Lett.* **95**, 226801 (2005).
- Kane, C. L. & Mele, E. J. Z_2 topological order and the quantum spin hall effect. *Phys. Rev. Lett.* **95**, 146802 (2005).
- Bernevig, B. A. & Zhang, S.-C. Quantum spin hall effect. *Phys. Rev. Lett.* **96**, 106802 (2006).
- Fu, L., Kane, C. L. & Mele, E. J. Topological insulators in three dimensions. *Phys. Rev. Lett.* **98**, 106803 (2007).
- Fu, L. Topological crystalline insulators. *Phys. Rev. Lett.* **106**, 106802 (2011).
- Ando, Y. & Fu, L. Topological crystalline insulators and topological superconductors: From concepts to materials. *Annu. Rev. Condens. Matter Phys.* **6**, 361–381 (2015).
- Benalcazar, W. A., Bernevig, B. A. & Hughes, T. L. Quantized electric multipole insulators. *Science* **357**, 61–66 (2017).
- Xie, B. et al. Higher-order band topology. *Nat. Rev. Phys.* **3**, 520–532 (2021).
- Schindler, F. et al. Higher-order topological insulators. *Sci. Adv.* **4**, eaat0346 (2018).

13. Trifunovic, L. & Brouwer, P. W. Higher-order bulk-boundary correspondence for topological crystalline phases. *Phys. Rev. X* **9**, 011012 (2019).
14. Ran, Y., Zhang, Y. & Vishwanath, A. One-dimensional topologically protected modes in topological insulators with lattice dislocations. *Nat. Phys.* **5**, 298–303 (2009).
15. Liu, C.-X., Zhang, R.-X. & VanLeeuwen, B. K. Topological non-symmorphic crystalline insulators. *Phys. Rev. B* **90**, 085304 (2014).
16. Hamasaki, H., Tokumoto, Y. & Edagawa, K. Dislocation conduction in Bi-Sb topological insulators. *Appl. Phys. Lett.* **110**, 092105 (2017).
17. Nayak, A. K. et al. Resolving the topological classification of bismuth with topological defects. *Sci. Adv.* **5**, eaax6996 (2019).
18. Kim, H. W. et al. Symmetry dictated grain boundary state in a two-dimensional topological insulator. *Nano Lett.* **20**, 5837–5843 (2020).
19. Juričić, V., Mesáros, A., Slager, R.-J. & Zaanen, J. Universal probes of two-dimensional topological insulators: Dislocation and π Flux. *Phys. Rev. Lett.* **108**, 106403 (2012).
20. Slager, R.-J., Mesáros, A., Juričić, V. & Zaanen, J. Interplay between electronic topology and crystal symmetry: Dislocation-line modes in topological band insulators. *Phys. Rev. B* **90**, 241403(R) (2014).
21. Roy, B. & Juričić, V. Dislocation as a bulk probe of higher-order topological insulators. *Phys. Rev. Res.* **3**, 033107 (2021).
22. Slager, R.-J., Juričić, V., Lahtinen, V. & Zaanen, J. Self-organized pseudo-graphene on grain boundaries in topological band insulators. *Phys. Rev. B* **93**, 245406 (2016).
23. Amudsen, M. & Juričić, V. Grain-boundary topological superconductor. *Commun. Phys.* **6**, 232 (2023).
24. Salib, D. J., Juričić, V. & Ro, B. Emergent metallicity at the grain boundaries of higher-order topological insulators. *Sci. Reps.* **13**, 15308 (2023).
25. Ko, W., Ma, C., Nguyen, G. D., Kolmer, M. & Li, A.-P. Atomic-scale manipulation and in situ characterization with scanning tunneling microscopy. *Adv. Funct. Mater.* **29**, 190377 (2019).
26. Li, W. & Li, J. Ferroelasticity and domain physics in two-dimensional transition metal dichalcogenide monolayers. *Nat. Commun.* **7**, 10843 (2016).
27. Su, W. P., Schrieffer, J. R. & Heeger, A. J. Solitons in polyacetylene. *Phys. Rev. Lett.* **42**, 1698 (1979).
28. Li, L., Xu, Z. & Chen, S. Topological phases of generalized Su-Schrieffer-Heeger models. *Phys. Rev. B* **89**, 085111 (2014).
29. Young, S. M. & Kane, C. L. Dirac semimetals in two dimensions. *Phys. Rev. Lett.* **115**, 126803 (2015).
30. Chiu, C. K., Teo, J. C., Schnyder, A. P. & Ryu, S. Classification of topological quantum matter with symmetries. *Rev. Mod. Phys.* **88**, 035005 (2016).
31. Nilus, N., Wallis, T. M. & Ho, W. Development of one-dimensional band structure in artificial gold chains. *Science* **297**, 1853 (2002).
32. Do, E. H. & Yeom, H. W. Electron quantization in broken atomic wires. *Phys. Rev. Lett.* **115**, 266803 (2015).
33. Howard, S. et al. Evidence for one-dimensional chiral edge states in a magnetic Weyl semimetal $\text{Co}_3\text{Sn}_2\text{S}_2$. *Nat. Commun.* **12**, 4269 (2021).
34. Gu, M. S. et al. Electric field-assisted patterning of few-layer MoTe_2 by scanning probe lithography. *J. Kor. Phys. Soc.* **82**, 274 (2023).
35. Hughes, H. P. & Friend, R. H. R. H. Electrical resistivity anomaly in $\beta\text{-MoTe}_2$. *J. Phys. C: Solid State Phys.* **11**, L103 (1978).
36. Rano, B. R., Syed, M. I. & Naqib, S. H. Ab initio approach to the elastic, electronic, and optical properties of MoTe_2 topological Weyl semimetal. *Alloy. Compd.* **39**, 154522 (2020).
37. Schindler, F. et al. Higher-order topology in bismuth. *Nat. Phys.* **14**, 918–924 (2018).
38. Noguchi, R. et al. Evidence for a higher-order topological insulator in a three-dimensional material built from van der Waals stacking of bismuth-halide chains. *Nat. Mater.* **20**, 473–479 (2021).
39. Kresse, G. & Furthmüller, J. Efficiency of Ab-initio total energy calculations for metals and semiconductors using a plane-wave basis set. *Comp. Mater. Sci.* **6**, 15–50 (1996).
40. Kresse, G. & Furthmüller, J. Efficient iterative schemes for ab initio total-energy calculations using a plane-wave basis set. *Phys. Rev. B* **54**, 11169–11186 (1996).
41. Perdew, J. P., Burke, K. & Ernzerhof, M. Generalized gradient approximation made simple. *Phys. Rev. Lett.* **77**, 3865–3868 (1996).
42. Perdew, J. P., Burke, K. & Ernzerhof, M. Generalized gradient approximation made simple. *Phys. Rev. Lett.* **78**, 1396–1396 (1997).
43. Kresse, G. & Joubert, D. From ultrasoft pseudopotentials to the projector augmented-wave method. *Phys. Rev. B* **59**, 1758–1775 (1999).

Acknowledgements

This work was supported by the National Research Foundation of Korea (NRF) grant funded by the Korea government (MSIT) (Grants No. RS-2023-00218998). M.J.P. was supported by the Institute for Basic Science in the Republic of Korea through the project IBS-RO24-D1.

Author contributions

H.W.K. and M.J.P. proposed and designed the research. W.-J. J, H.N. and H.W.K. carried out the STM experiments. H.W.K. and W.-J. J analyzed the STM data. S.-H.K. and J.K. performed the DFT calculations. M.J.P. developed the theoretical model. M.J.P, H.W.K, W.K. and S.-H. K wrote the manuscript. All authors have read and approved the final version of the manuscript.

Competing interests

The authors declare no competing interests.

Additional information

Supplementary information The online version contains supplementary material available at <https://doi.org/10.1038/s41467-024-53315-0>.

Correspondence and requests for materials should be addressed to Moon Jip Park or Hyo Won Kim.

Peer review information *Nature Communications* thanks the anonymous, reviewer(s) for their contribution to the peer review of this work. A peer review file is available.

Reprints and permissions information is available at <http://www.nature.com/reprints>

Publisher's note Springer Nature remains neutral with regard to jurisdictional claims in published maps and institutional affiliations.

Open Access This article is licensed under a Creative Commons Attribution-NonCommercial-NoDerivatives 4.0 International License, which permits any non-commercial use, sharing, distribution and reproduction in any medium or format, as long as you give appropriate credit to the original author(s) and the source, provide a link to the Creative Commons licence, and indicate if you modified the licensed material. You do not have permission under this licence to share adapted material derived from this article or parts of it. The images or other third party material in this article are included in the article's Creative Commons licence, unless indicated otherwise in a credit line to the material. If material is not included in the article's Creative Commons licence and your intended use is not permitted by statutory regulation or exceeds the permitted use, you will need to obtain permission directly from the copyright holder. To view a copy of this licence, visit <http://creativecommons.org/licenses/by-nc-nd/4.0/>.

© The Author(s) 2024